

# Channel State Information Based Human Presence Detection using Non-linear Techniques

Sameera Palipana<sup>1,\*</sup>, Piyush Agrawal<sup>2</sup> and Dirk Pesch<sup>1</sup>

<sup>1</sup>Nimbus Centre, Cork Institute of Technology, Ireland

<sup>2</sup>United Technologies Research Centre, Cork, Ireland

\*Contact Author: dhanapala.palipana@mycit.ie

## ABSTRACT

Channel State Information (CSI) obtained from commercial Wi-Fi chipsets has proven to be efficient in detecting human interaction with radio waves. However, there is a lack of analytical modelling to define the impact of human presence on multidimensional CSI vectors. Existing approaches include linear, parameter-less techniques to reduce signal space dimensions and filter noise by assuming linear correlations among sub-carriers.

In this work, we first model the human presence and then analyse occurrences of non-linear correlations among sub-carriers. We then exploit these correlations by introducing non-linear techniques to reduce CSI dimensions and filter noise. These techniques offer adjustable parameters that enhance signal quality depending on the environment and the amount of human interaction. We analyse the performance of human presence detection using the introduced techniques with just two transceivers. Our results show that when human motion is insignificant or occurs far from the link, non-linear techniques improve the detection accuracy up to 5% compared to the linear approach.

## CCS Concepts

•**Hardware** → **Signal processing systems**; *Wireless devices*; •**Networks** → Wireless access points, base stations and infrastructure;

## Keywords

device-free, CSI, human presence

## 1. INTRODUCTION

Information on human presence in buildings plays an important role in controlling energy consumption of Heating Ventilating and Air Conditioning (HVAC) and lighting systems. Detection of human presence is also critical for building surveillance, automation, assisted living services and the likes. Furthermore, it is a key element in providing higher

level contextual information such as locations, activities, gestures and identities in indoor environments.

Among the traditional technologies that detect human presence, Passive Infra-Red (PIR), cameras, CO<sub>2</sub> sensors, and radio waves are popular approaches [1, 2]. However, PIR sensors experience low range, require multiple sensors to achieve a reliable detection and the detection accuracy is low for static persons. Cameras are intrusive of privacy [3] and have issues in penetrating walls, darkness and smoke [4]. CO<sub>2</sub> sensors have particularly slow response time. Technologies such as radar, ultrawideband and Wi-Fi Channel State Information (CSI) obtained through SDR-based solutions are reliable but expensive.

The popularity of approaches that measure Received Signal Strength (RSS) by narrowband radio devices is due to cost effectiveness and ubiquity. However, recent progress in signal descriptors, such as CSI, obtained through low cost IEEE 802.11n chipsets offer enhanced accuracy compared to RSS. Due to high temporal variance in RSS, slow movements of humans end up hidden in the inherent signal variability [5]. Comparatively, the structure of CSI is temporally more stable than RSS because it captures small-scale multipath propagation over multiple sub-carriers in frequency domain [6, 7]. CSI indicates different physical qualities of the channel such as shadowing, frequency selective fading, multipath propagation and effects of interference. Hence, CSI is currently a good alternative for RSS.

Compared to traditional technologies, CSI-based detection has several advantages. It detects humans through walls, does not depend on lighting, preserves user privacy, and importantly, occupants are not required to carry any devices. Hence, it is widely used to quantify the human presence interaction with the wireless channel in the form of occupancy detection, activity/gesture/identity recognition and human positioning.

**Prior work and their limitations.** Currently, models for human influence on RSS amplitude variations exist for narrowband radio devices. However, models that characterise sub-carrier level amplitude variations in CSI are non-existent to the best of our knowledge. Previous human presence detection schemes assumed that CSI sub-carriers are correlated in the empty environment. They also assumed a loss of correlation with human presence. Therefore, reduction of CSI dimensions was performed using linear methods such as eigen-decomposition of the CSI correlation matrix. These techniques are parameterless and adapting them to different environments with different noise profiles is a difficult problem to tackle. Especially when the human is mostly static,

Permission to make digital or hard copies of all or part of this work for personal or classroom use is granted without fee provided that copies are not made or distributed for profit or commercial advantage and that copies bear this notice and the full citation on the first page. Copyrights for components of this work owned by others than ACM must be honored. Abstracting with credit is permitted. To copy otherwise, or republish, to post on servers or to redistribute to lists, requires prior specific permission and/or a fee. Request permissions from [permissions@acm.org](mailto:permissions@acm.org).

*BuildSys'16 November 16-17, 2016, Palo Alto, CA, USA*

© 2016 ACM. ISBN 978-1-4503-4264-3/16/11...\$15.00

DOI: <http://dx.doi.org/10.1145/2993422.2993579>

these approaches can have low detection effectiveness.

**Contributions.** The specific contributions of our work are: (i) we provide a model to characterise sub-carrier amplitude variation of the CSI with human presence. Using this model we explain the non-linearities that can occur in CSI under the influence of humans. (ii) We introduce a novel dimensionality reduction and noise filtering scheme. We exploit the identified non-linearities in CSI under human influence and use a non-linear technique, kernel Principal Component Analysis (kPCA), to reduce dimensions. kPCA kernels offer adjustable parameters that help in reducing noise to suit different environments. (iii) Furthermore, we focus on a mostly static occupant and achieve enhanced detection accuracy for humans with small movements using just two Wi-Fi transceivers.

The remainder of this paper is organised as follows. Section 2 provides a summary of existing CSI-based human presence characterization models and human presence detection techniques. Section 3 introduces our model which defines CSI amplitude variation due to human motion. In Section 4 we introduce our technique on CSI dimensionality reduction and our human presence detection scheme. We then describe our experimental environment, data collection and evaluation of our presence detection scheme in Section 5. We discuss the scope and limitations of this work in Section 6 and provide our conclusions in Section 7.

## 2. RELATED WORK

As our paper introduces a model and a detection technique for human presence, this section is divided into two parts to address the current relevant state of the art considering these two aspects.

### 2.1 Models on Human Presence

There is a lack of models in the literature to represent the effect of human presence on CSI amplitude and phase. However, human presence models that have been developed for other narrowband devices using RSS can be adapted to model CSI fluctuations. Among RSS-based models, Patwari and Wilson [8, 9] introduced a link centric, statistical model to express RSS variation detected with narrowband devices as a function of a person’s position. They separated total received paths as affected and unaffected and derived expressions for the total affected power due to affected paths. Among CSI-based models, Omni-PHD [6] extended the link centric model to a near disk like coverage model around the receiver using CSI as the measurement. The authors determined whether a person is within a near-disk region or not, with similar confidence levels. CARM [10] introduced a link centric, deterministic model to characterise the human movement speed on CSI for activity recognition by separating the affected and unaffected components.

Our work is different to these approaches in that we characterise the variation of CSI amplitude of each sub-carrier depending on a human’s position using the affected and unaffected components.

### 2.2 Human Presence Detection Schemes

Previous device-free human presence detection approaches that use CSI as the signal descriptor are twofold: threshold-based and fingerprint-based.

**Fingerprint-based.** In this approach, a distance measure between a CSI fingerprint during human motion and the un-

occupied room characterises human availability. Pilot [11] measured the cross-correlation as the distance measure, and [12] extended it to an adaptive method depending on the environment. In [13] grey relational analysis was used to measure the distance. Omni-PHD [6, 14] used a statistical approach and the fingerprint is a histogram of CSI amplitudes where Earth Mover’s distance [15] measures the distance between unoccupied and occupied histograms. The intuition in these methods is that the affected multi-paths due to human motion would create enough perturbations in CSI vectors to reduce the similarity between unoccupied and occupied fingerprints.

**Threshold-based.** Threshold-based approaches exploit the high linear temporal correlation among CSI amplitudes for an unoccupied room. They distinguish the occupied room assuming a loss of correlation in CSI due to temporal amplitude variations. These techniques perform eigen decomposition on the CSI correlation matrix for two reasons, (i) to reduce the dimensions and noise in CSI, and (ii) to separate the unoccupied room from the occupied with the intuition that eigenvalue variation indicates motion. FIMD [7] first leveraged the correlation among sub-carrier amplitudes to detect human *motion*. They used first and second eigenvalues to separate the unoccupied room from the occupied using a threshold. PADS [16] and DeMan [17] extended the motion detection to phase and amplitude of CSI by assuming linear correlation among sub-carriers. They used the first eigenvalue of both amplitude and phase and determined the threshold of unoccupied and occupied scenarios in these two cases by a support vector machine classifier. Although these methods were using the first eigenvalue in detection, it was later proved to be unreliable due to burst noise [10]. This can hinder the detection accuracy especially when humans are static. Nonetheless, these schemes were focusing mainly on detecting a moving person.

In DeMan [17] a static occupant was detected through their breathing. It uses the power spectral density of subcarrier amplitudes and identifies frequencies related to breathing. However, this approach is constrained by the detection range due to transmit power limitations.

Similar to the above, we perform threshold-based detection using eigen-decomposition. However, we try to solve the problem by exploiting non-linearities among sub-carriers and we are different to the rest in three aspects, (i) we use our model to first explain the non-linearities caused by human presence and then we exploit them in our dimensionality reduction technique, (ii) our techniques are parameter-based, so they are adaptable to different environments, and (iii) we focus on detecting a person who is mostly static resembling real world situations.

## 3. MODELLING HUMAN PRESENCE

In this section, we initially provide an introduction to Channel State Information (CSI) then we present our model and its validation. Then we use the model to explain the non-linearities in CSI.

### 3.1 CSI Preliminaries

In wireless radio propagation, radio waves arrive at the receiver over multiple paths due to reflection, diffraction and scattering caused by objects in the environment. The received signal can be characterised by channel impulse re-

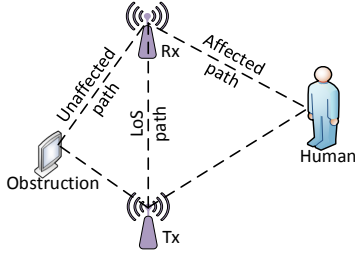


Figure 1: The behaviour of affected and unaffected paths due to human influence.

sponse  $h(t; \tau)$  [18],

$$h(t; \tau) = \sum_{i=0}^{M-1} a_i(t) e^{j\phi_i} \delta(t - \tau_i(t)) \quad (1)$$

where  $a_i(t)$  is the amplitude of the  $i^{\text{th}}$  path,  $\phi_i$  is the total phase shift caused by physical propagation phenomena such as reflections and diffractions,  $\tau_i(t)$  is the time varying delay of  $i^{\text{th}}$  path and  $M$  is the number of paths. However, due to bandwidth limitations, Wi-Fi receivers can only distinguish clusters of multipath components [19].

The frequency domain representation of  $h(t; \tau)$  is the channel frequency response  $H(t; f)$  [10, 20]:

$$H(t; f) = \sum_{i=0}^{M-1} a_i(t) e^{j\phi_i} e^{-j2\pi f \tau_i(t)} \quad (2)$$

Wi-Fi devices that operate in IEEE 802.11a/g/n/ac use Orthogonal Frequency Division Multiplexing (OFDM) as the modulation scheme with multiple sub-carriers in a Wi-Fi channel to send data. The receiver measures a discrete Channel Frequency Response (CFR) in time and frequency as phase and amplitude in the form of CSI for each antenna pair:

$$H(t; f) = [H(t; f_1), H(t; f_2) \dots H(t; f_n)] \quad (3)$$

where  $H(t; f_i) = \|H(t; f_i)\| e^{j\angle H(t; f_i)}$  and  $n$  is the number of sub-carriers.

### 3.2 Modelling the CFR in Human Presence

The purpose of this section is to model and derive expressions for *amplitude* measurements  $\|H(t; f_i)\|$  of CSI sub-carriers obtained from the IWL 5300 Wi-Fi chipsets that depend on a person's position.

The effect of human presence on radio waves can be classified into two groups as *unaffected*: paths that are not affected by the person, and *affected*: paths that have changes in amplitude, phase and delay due to human presence and new paths that are generated due to scattering and reflection off the person. This behaviour is illustrated in Figure (1). Hence, the resultant channel in eq. 2 can be expressed as just two components, as unaffected  $H_u(f)$  and affected  $H_a(t; f)$  [9, 10]:

$$H(t; f) = H_u(f) + H_a(t; f) \quad (4)$$

$H_u(f)$  consists of  $N$  unaffected paths. We assume the unaffected paths to have fixed lengths, the amplitude  $a_i$  and phase  $\phi_i - 2\phi f \tau_i$  are time invariant:

$$H_u(f) = \sum_{i=0}^{N-1} a_i e^{j\phi_i} e^{-j2\pi f \tau_i} \quad (5)$$

$H_a(t; f)$  consists of  $M - N$  affected time varying paths:

$$H_a(t; f) = \sum_{i=N}^{M-1} a_i(t) e^{j\phi_i} e^{-j2\pi f \tau_i(t)} \quad (6)$$

As human movements cause affected path lengths to change, amplitudes and phases of these paths are time varying.

**Modelling the unaffected component.** The unaffected component,  $H_u(f)$  in our work is modelled as follows.  $H_u(f)$  consists of largely the specular Line of Sight (LoS) paths and the paths resulted from reflections and scattering off static objects. Hence, we approximate  $H_u(f)$  by the CSI observed in the absence of a person in the room,  $H_e(f)$  with amplitude  $a_e(f)$  and phase  $\phi_e(f)$ :

$$H_u(f) \approx H_e(f) = a_e(f) e^{j\phi_e(f)} \quad (7)$$

**Modelling affected component.** Modelling of the unaffected component in our work is done as follows. Due to peculiarities of human bodies, the set of affected paths can consist of a single  $N_s = 1$  or multiple  $N_s > 1$  specular paths and a collection of diffused paths  $N_d \gg 1$  with small amplitudes and random phases. For simplicity, we assume that there is a single specular path with amplitude  $a_s(t)$  and delay  $\tau_s(t)$ , which is reflected by the person. To account for the variations caused by the diffused paths,  $a_s(t)$  can be modelled as a Rician random process. Furthermore, we assume that the occupant does not obstruct the LoS paths. LoS obstructions cause high variations in the sub-carriers due to shadowing and diffraction. These effects are not considered here because we are more concerned about the effect on the CFR due to subtle indirect movements. Therefore, eq. 6 reduces as follows:

$$H_a(t; f) \approx a_s(t) e^{-j2\pi f \tau_s(t) + j\phi_s} \quad (8)$$

In reality,  $H_a(t; f)$  is a time varying result of body scattering and/or reflections that depend on the position of the person. Therefore, by applying Friis path loss equation, the specular amplitude  $a_s(t)$  of the reflected paths can be modelled as [8]:

$$a_s(t) = \frac{kd_0 \sqrt{P_{rx}}}{\|x_{tx} - x(t)\| + \|x_{rx} - x(t)\|} \quad (9)$$

where  $d_0$  is the link length,  $x(t)$  is the coordinate of the person,  $x_{tx}$  and  $x_{rx}$  are the coordinates of the transmitter and the receiver and  $k$  is the reflection loss and  $P_{rx}$  is the received power. Due to the person's trajectory, phase shift caused by change of the reflected path length  $f\tau_s(t)$  in eq. 8 can be written as:

$$f\tau_s(t) = \frac{f \times (\|x(t) - x_t\| + \|x_r - x(t)\|)}{c} \quad (10)$$

where  $c$  is the speed of light.

**Amplitude response model.** From eq. 7 and eq. 8 we obtain the overall channel frequency response  $H(t; f)$  and our intended result  $\|H(t; f_i)\|$  by substituting the sub-carrier frequencies  $f_i$ . Therefore, the amplitude response  $\|H(t; f_i)\|$  of the  $i^{\text{th}}$  sub-carrier with AWGN noise  $N(o, \sigma_{amp})$  is:

$$\|H(t; f_i)\| = \left[ a_e^2(f_i) + a_s^2(t) + 2a_e(f_i)a_s(t) \cos(2\pi f_i \tau_s(t) + \phi_{se}(f_i)) \right]^{\frac{1}{2}} + N(o, \sigma_{amp}) \quad (11)$$

The implementation of CSI in the IWL 5300 chipset does not include noise measurements on a per sub-carrier basis

Table 1: Model Parameters.

Parameter	Value	Parameter	Value
TX rate	1000 pkts <sup>-1</sup>	TX power	15 dBm
Human speed	0.8 ms <sup>-1</sup>	Duration	5 s
Link length ( $d_0$ )	5 m	SNR	100 dB
Reflect. attn. ( $k$ )	6	Channel BW	20 Mhz
Carrier freq.	5.32 GHz	Antennas	1 × 1

[21], so we assume that the noise floor is uniform across all sub-carriers. Through CSI amplitudes received during the presence and absence of a person in a real world experiment, the amplitude response of the above model can be validated. We provide our validation procedure in Section 3.3.

The phase response is not verifiable from the current state of CSI provided by the IWL 5300 chipset. These off-the-shelf WiFi devices produce Carrier Frequency Offsets (CFO) due to small carrier frequency differences in the transmitting and receiving radios leading to phase randomness in CSI among successive packets [10, 22]. Although there is a calibration method to overcome phase randomness, the actual phase is not recoverable through this approach [23].

### 3.3 Model Validation

To validate the model's behaviour during the presence of a single person, we carried out an experiment where a person moves towards the direct LoS link in a perpendicular trajectory from 4 m away. As shown in Figure 2, the person's movement is important in this case to understand its impact on sub-carrier amplitudes. Since we assume a constant reflection attenuation ( $k$ ) of the reflected path, the best movement to achieve a sufficiently constant reflection attenuation is walking perpendicular to the link where the person's chest is facing the link. The used model parameters are summarized in Table 1. The impact of human motion on sub-carrier 1 is compared to the real experiment results in Figure 3. The top figure corresponds to the model result and the bottom one represents the real fluctuations in the sub-carrier.

In the experiment, the person starts his movement towards the link from 4 m away at 0 s. When the person is far from the link, the fluctuations in the sub-carrier are small and have a high frequency, whereas closer to the link the fluctuations are large and have a lower frequency. This is caused by the length reduction of the reflected path as the person moves in during this period. The model follows the real pattern until 4.5 s. From there onwards, there is a large difference between modelled and real values. This is due to the shadowing of the LoS path by the human which is not modelled in our case.

The amplitude of the real sub-carrier has high variations compared to the modelled amplitude. This is caused by vari-

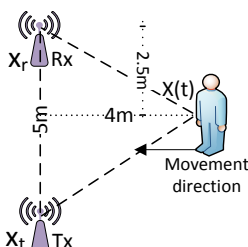


Figure 2: Person's position and trajectory during the experiment.

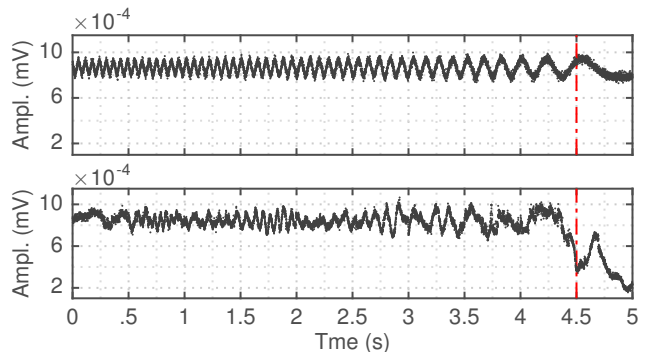


Figure 3: Modelled (top) and real (bottom) sub-carrier amplitude variation.

ation of the attenuated reflection ( $k$ ) of the reflected path due to movement. In the model, this attenuation is predetermined through a training experiment and assumed constant over time. The other discrepancy between the model and actual result is the phase shift which is a result of a combination of factors such as initial phase of the unoccupied room  $\phi_e(f)$ , reflections and the fluctuation in human velocity.

In order to quantify the similarity between the real  $H_r$  and the modelled  $H_m$  CSI matrices, we measured the cross correlation,  $-1 < \rho(H_m, H_r) < 1$ :

$$\rho(H_m, H_r) = \frac{\text{cov}(H_m, H_r)}{\sigma_m \sigma_r} \quad (12)$$

where  $\text{cov}(H_m, H_r)$  is the covariance between  $H_m$ ,  $H_r$  and  $\sigma_m$ ,  $\sigma_r$  are the standard deviations of  $H_m$  and  $H_r$  respectively. Both matrices are of size  $(30) \times (\text{TX rate} \times 4.5)$  where 30 is the number of sub-carriers, TX rate = 1000 pkts<sup>-1</sup> and 4.5 is the duration in seconds without the shadowing period. We obtained a cross correlation of 0.9 between the two matrices. We needed this model to understand the parameters that affect the sub-carriers due to human influence. Hence, for the mentioned purpose, this accuracy is quite adequate.

### 3.4 Sources of Non-Linearities

In this section, we argue that most sub-carrier amplitudes have a non-linear temporal correlation that originate through several sources. We use our model in eq. 11 to identify those sources.

The main sources of non-linearities are: (i) human motion, expressed through  $a_s(t)$  and  $\tau_s(t)$  (ii) the amplitude  $a_e(f)$  and phase  $\phi_e(f)$  of the channel frequency response of the empty environment (higher non-linearities can occur in a cluttered environment due to an increase of peaks and valleys in the amplitude response caused by multipath propagation) (iii) measurement duration  $t$ . If multiple antennas are used, sub-carriers across these antennas also tend to get non-linearly correlated as the measurement duration increases. To a lesser extent, this is true for the sub-carriers among same antenna as well. Additionally, amplitude and phase response of each sub-carrier is non-linearly correlated.

We verify these findings from the data collected during the experiment for model validation in Section 3.3. As an example, the correlation matrix  $\mathbf{H}$  of size  $90 \times 90$  (90 sub-carriers from 1 × 3 antennas) of the measured data can be calculated as:

$$\mathbf{H} = \mathbf{X}\mathbf{X}^T \quad (13)$$

where  $\mathbf{X}$  is the observation matrix of size  $90 \times N_s$ .  $N_s$  is

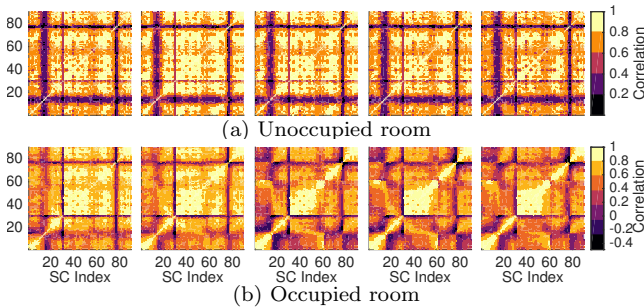


Figure 4: The top row represents the correlation matrix of the unoccupied room  $\mathbf{H}_{empty}$  and the bottom one corresponds to the correlation matrix at human presence  $\mathbf{H}_{occu}$ .  $N_s = 1000i, 2000i, \dots, 5000i$ , where  $i$  is the column index.

the number of samples from the experiment we used to validate the model and it represents the measurement duration  $t$ ,  $N_s = t \times TXrate$ . The results of the calculation are illustrated in Figures 4a and 4b for unoccupied and occupied rooms respectively.

As observed in the figures, the occupied room loses the correlation after 2s ( $N_s = 2000$ ). The highest correlation in the occupied room is mostly concentrated among nearby sub-carriers of the same antenna which corresponds to the yellow colour in the bottom five figures. Additionally, as  $N_s$  increases, the non-linearities increase, whereas for the unoccupied room, sub-carrier correlation is almost constant over time. The *dark brown* coloured lines in the unoccupied room figures correspond to the valleys in the CFR amplitude. Therefore, the more cluttered the environment, the more valleys we can observe, which results in non-linearities.

## 4. DIMENSIONALITY REDUCTION AND HUMAN PRESENCE DETECTION

In this section we devise a system to efficiently exploit the non-linear correlations among the sub-carriers that were mentioned in Section 3.4 in order to reduce the dimensions, filter noise and detect human presence.

### 4.1 System Overview

The system architecture of our detection scheme is illustrated in Figure 5. As shown, when CSI is extracted from the packets received through the link, we first linearly interpolate them to account for packet losses and achieve a fixed rate. Then, nonlinear dimensionality reduction, specifically, kPCA is applied to this data and obtain a single temporally fluctuating signal by selecting the optimum principal component and its respective eigenvalue. Finally, presence detection is performed by setting a threshold to this eigenvalue depending on the environment.

### 4.2 Linear Approach: PCA

For a Wi-Fi data packet received by a single antenna pair, a CSI amplitude vector provides  $30 \times 1$  dimensions. An IEEE 802.11n implementation can use up to  $3 \times 3$  antenna pairs where dimensions of a CSI data point can reach up to  $270 \times 1$ . It is a cumbersome process to set 270 thresholds for each dimension in order to distinguish the unoccupied room from the occupied. Besides, each CSI sub-carrier contains noise, which also requires filtering. Hence, we require a mechanism to successfully reduce the dimensions or identify the highest varying dimensions. Additionally, the re-

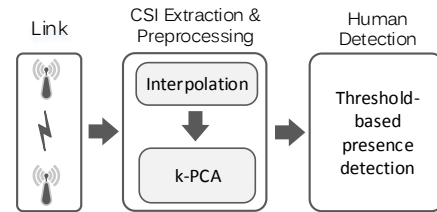


Figure 5: Human presence detection scheme. System overview.

duced dimensions also need to contain less noise. A method used in the literature to achieve this assuming linear correlation among sub-carriers is principal component analysis (PCA) [10]. Although PCA is not part of our work, we explain it here briefly because our approach in Section 4.3 is a generalisation of this technique.

Mathematically, the number of CSI amplitudes  $N_{obs}$  obtained from  $N_{obs}$  packets can be expressed as a  $\mathcal{D} \times N_{obs}$  matrix  $\mathbf{X}$ , where  $\mathcal{D}$  is the number of subcarriers. PCA assumes that rows of this matrix are linearly correlated. It then linearly transforms the rows to a new orthogonal coordinate system. This is done by eigendecomposition of the correlation matrix  $\mathbf{K}^{PCA}$  of  $\mathbf{X}$ :

$$\mathbf{K}^{PCA} = \mathbf{X}^T \mathbf{X} = \mathbf{V} \mathbf{\Lambda} \mathbf{V}^{-1} \quad (14)$$

Eigenvectors  $\{\mathbf{v}_i \in \mathcal{R}^{N_{obs}} \mid i = 1, 2, \dots, \mathcal{D}\}$  form the new directions of the coordinate system. The variances of the new directions are captured by the eigenvalues  $\{\lambda_i \in \mathcal{R} \mid i = 1, 2, \dots, \mathcal{D}\}$  where  $\lambda_1$  has the highest variance. Principal Components ( $PCs$ )  $y_i$ , where  $y_i = \mathbf{K}^{PCA} \times \mathbf{v}_i$  are the coordinates of the new data points. Since the first  $PC$ ,  $y_1$  contains the majority of variation in the signal, it has a higher signal to noise ratio. Therefore, using the variance/eigenvalue of this  $PC$  or another  $PC$  that has the signal portion, we can separate the unoccupied room from the occupied.

### 4.3 Non-Linear Approach: kPCA

We use kPCA [24] in our work to exploit the non-linear correlations in CSI. kPCA first transforms the data to a higher dimensional space and then performs the eigendecomposition to reduce the dimensions as in the previous section.

This is achieved by a non-linear transformation of the original data  $\{\mathbf{x}_i, \mathbf{x}_j \in \mathcal{R}^{\mathcal{D}} \mid i, j = 1, 2, 3, \dots, N_{obs}\}$  into a feature space  $\mathcal{F}$  using a function  $\phi$ :

$$\phi : \mathcal{R}^{\mathcal{D}} \rightarrow \mathcal{F}, \mathbf{x} \rightarrow \mathbf{X}$$

The feature space  $\mathcal{F}$  can be of a very high dimensionality. Therefore, without explicitly knowing the transformation function  $\phi$ , Mercer kernels [25] can be used to transform the data [25]. Using a Mercer kernel is analogous to knowing the dot product of the transformed data points  $K_{ij} = \kappa(\mathbf{x}_i, \mathbf{x}_j) = \phi(\mathbf{x}_i) \cdot \phi(\mathbf{x}_j)$ ,  $\mathbf{K} : \mathcal{R}^{\mathcal{D}} \times \mathcal{R}^{\mathcal{D}} \rightarrow R$ .

Kernels that have been useful in kPCA include Gaussian and polynomial kernels [25]. In this work, we use both these kernels to non-linearly transform our data to a higher dimension. In Sections 4.3.1 and 4.3.2 we explain the reasons for selecting them and the transformation procedure. After transforming the data using the selected kernel, eigendecomposition is performed similar to linear PCA to obtain the principal components and the respective eigenvalues. We implemented this according to the procedure mentioned in [26].

After sorting the eigenvalues and respective principal components in descending order of the eigenvalues, we choose

the best *PCs* for human presence detection. The selection procedure and actual detection is explained in Section 4.4.

### 4.3.1 Gaussian Kernel

In this section, we explain the reasons for choosing this kernel and how the parameters were tuned to suit our data. eq. 15 represents the Gaussian kernel used in this work:

$$\kappa(\mathbf{x}_i, \mathbf{x}_j) = e^{-\frac{\|\mathbf{x}_i - \mathbf{x}_j\|^2}{\sigma}} \quad (15)$$

where  $\sigma$  is the standard deviation which is a tunable parameter, and  $\|\mathbf{x}_i - \mathbf{x}_j\|$  is the Euclidean distance between two data points  $\mathbf{x}_i, \mathbf{x}_j$ . This is the most commonly used non-linear kernel in kPCA and here we summarize the reasons for selecting it:

1. Frequency domain representation of the Gaussian kernel is also Gaussian, so it does not introduce high frequency non-linearities. Hence, it provides smooth principal components through transformation [27]. Therefore, when expert knowledge about the non-linearities is lacking, the Gaussian kernel offers a reliable solution under general smoothness assumption.
2. The width of the Gaussian kernel  $\sigma$  can be adjusted depending on the type of data to filter out noise, which will be explained below.

**Parameter optimisation.** The standard deviation  $\sigma$  of the Gaussian kernel was optimised for our data as follows.

We ran a set of experiments for two different types of scenarios, e.g. unoccupied and occupied room as described in Section 5, in order to show how we determine  $\sigma$  for the Gaussian kernel. We obtained two data sets of size 3000, one each for unoccupied and occupied room experiments. Then we plot the Gaussian transformation of median Euclidean distance of both data sets and plot them in Figure 6 against the standard deviation  $\sigma$ . The figure illustrates the variation of  $f(\sigma)$  vs.  $\sigma$  where  $f(\sigma) = e^{-\frac{Md(\|\mathbf{x}_i - \mathbf{x}_j\|^2)}{\sigma}}$  and  $Md(\|\mathbf{x}_i - \mathbf{x}_j\|^2)$  is the median Euclidean distance of 3000 data points.

The median Euclidean distance is considered instead of the mean because it is better in describing the central tendencies of the two data sets when the distribution of Euclidean distances are skewed. Unoccupied room data points usually have a low Euclidean distance because this environment causes low perturbations in the signal and these perturbations are predominantly caused by noise. Therefore, if we have a fixed  $\sigma$  for the two data sets, the Gaussian transformation of the Euclidean distance of the unoccupied room data gives high variations compared to the occupied. Hence, we require a mechanism to update  $\sigma$  depending on the nature of our data.

From Figure 6 we know that median Euclidean distance  $Md(\|\mathbf{x}_i - \mathbf{x}_j\|^2)$  provides some hint on the nature of data. From eq. 15 we also know that when  $\sigma$  is high, a data point after Gaussian transformation has larger influence on neighbour data points leading to low variation and noise in the principal components. On the other hand, when  $\sigma$  is low, data points have less influence on neighbour data points and this causes high variation and noise in the principal components. Hence, depending on the median Euclidean distance of the data, we can set a threshold,  $Eud_{th}$  to separate low Euclidean distances from high ones so that the low ones correspond to the unoccupied room. Depending on the threshold, we can set  $\sigma$  to a higher value (saturate region of the unoccupied  $f(\sigma_{unoccu})$  curve in Figure 6) for the unoccupied

room to suppress high variations. Since a high  $\sigma$  value for a data point has larger influence on neighbour data points, it cancels out the noise. To highlight variations in the occupied room,  $\sigma$  is set to a value (in the linear region of the occupied  $f(\sigma_{occu})$  curve in Figure 6) for Euclidean distances exceeding  $Eud_{th}$ .

### 4.3.2 Polynomial kernel

Eq. 16 describes the polynomial kernel used in kernel PCA where  $c$  and  $d$  are two adjustable parameters:

$$\kappa(\mathbf{x}_i, \mathbf{x}_j) = (\mathbf{x}_i^T \mathbf{x}_j + c)^d \quad (16)$$

The linear kernel used in PCA is a subset of the polynomial kernel. The polynomial kernel can be transformed to either linear or a higher order polynomial depending on the type of data by adjusting the parameter  $d$  in eq. 16. Higher order polynomials amplify higher amplitudes in the signal and suppresses lower amplitudes such as noise. However, unlike the Gaussian kernel, a polynomial kernel can distort the principal components through the transformation. Adjusting the parameters such as  $c$  and  $d$ , these distortions can be minimized. Below we show how the parameters are selected for the polynomial kernel in our approach.

**Parameter selection.** For the polynomial kernel in eq. 16 there are two parameters that can be adjusted ( $c, d$ ). For the choice of  $d$ , we kept  $d = 2$  so that this becomes a second order polynomial. For higher order polynomials we obtain very high eigenvalues and principal components especially when the occupant is moving. The computation time of higher order polynomials are also high. Therefore, eq. 16 reduces to:

$$\kappa(\mathbf{x}_i, \mathbf{x}_j) = (\mathbf{x}_i^T \mathbf{x}_j + c)^2 = (\mathbf{x}_i^T \mathbf{x}_j)^2 + 2c\mathbf{x}_i^T \mathbf{x}_j + c^2 \quad (17)$$

When the parameter  $c$  is high there is increased weight for lower order values, e.g.,  $2c\mathbf{x}_i^T \mathbf{x}_j$  which provides a smooth signal for both occupied and unoccupied rooms. When  $c$  is low, the weight on higher order values are high resulting in high peaks for the principal component when the occupant is moving. In our case, we set  $c = Md(\mathbf{x}_i^T \mathbf{x}_j)$  of data points of size  $N_{obs}$  so that we achieve a balanced signal without unnecessary peaks.

## 4.4 Human Presence Detection

In Section 4.3 we identified the highest varying principal components from the eigendecomposition of Gaussian and polynomial kernel transformed data. The purpose of this section is to determine the best PC and the respective eigenvalue and determine a threshold to detect human presence.

After applying kPCA, as mentioned in section 4.3 we obtain more dimensions than the original ones. We do not know how many *PCs* carry the signal component and how many *PCs* are just noise. To separate the signal components from the noise, we use a scree plot as in Figure 7. It plots the amplitude of each eigenvalue with its index. The point where the steep curve ends (marked with a red dashed line in the figure) is considered to be the last point where the signal portion is carried. For the particular case in the figure, the first four *PCs* can be selected as the best.

In both PCA and kPCA, *PC1* corresponds to the highest eigenvalue and captures the highest variance of the signal. However in CSI, the first principal component is unusable due to high noise. The reason is that *PC1* of the unoccupied room has high variation which reduces the overall signal to

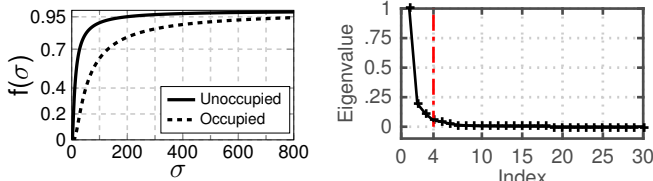


Figure 6:  $f(\sigma)$  vs  $\sigma$  of 3000 data points comparing unoccupied and occupied rooms.

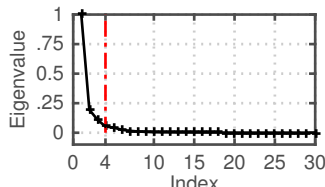


Figure 7: Screen plot.

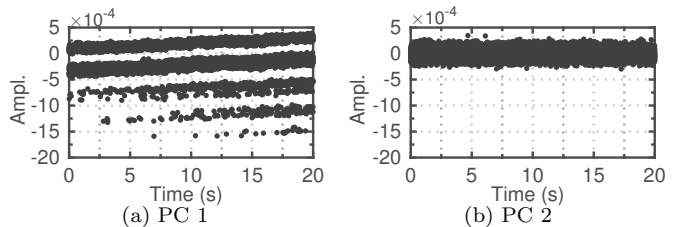


Figure 8: PCs of the empty room.

noise ratio of the occupied and unoccupied rooms. As an example, Figure 8 shows the temporal fluctuations of  $PCs$  1 and 2.  $PC1$  indicates a signal with multiple levels whereas  $PC2$  consists of a single level. We argue that these multiple levels are a result of multiple peaks and valleys of the CFR caused by frequency selective fading. Even though we subtract the mean of each subcarrier prior to applying kPCA, the mean subtracted CSI contains high variation in the subcarriers with peaks and low variation at valleys leading to multiple levels in  $PC1$ .

Therefore, for human presence detection, the best  $PC$  out of the above four  $PCs$  are chosen based on the maximum eigenvalue ratio  $\Lambda_{max}$  of empty and occupied scenarios:

$$\Lambda_{max} = \max_k \frac{\lambda_{k,occu}}{\lambda_{k,empty}} \text{ where } k = 1, 2, \dots, m \quad (18)$$

$PCs$  2 and 3 tend to maximize this ratio due to high signal power and low noise in those  $PCs$ . In Section 5.3.1 we show that the performance of  $PCs$  2 and 3 vary depending on the noise profile of the environment.

After selecting the best principal component for detection, separation of the empty scenario from an occupied scenario must be performed for the test data. This is done by setting a threshold for the training data obtained during the absence of a person in the unoccupied room. This threshold  $\lambda_{th}$  corresponds to the highest eigenvalue of the *selected* principal component from  $n$  intervals of the training period:

$$\lambda_{th} = \max_i (\lambda_{i,empty}), \text{ where } i = 1, 2, \dots, n \quad (19)$$

If an eigenvalue of test data exceeds this threshold, it is counted as a detection.

## 5. EVALUATION

In this section we explain our experimental environment, execution of the experiments and the obtained results.

### 5.1 Experimental Setup

The experiments were performed at a research lab in our centre and the floor plan is given in Figure 9. We collected data from two experiments A, B corresponding to the link

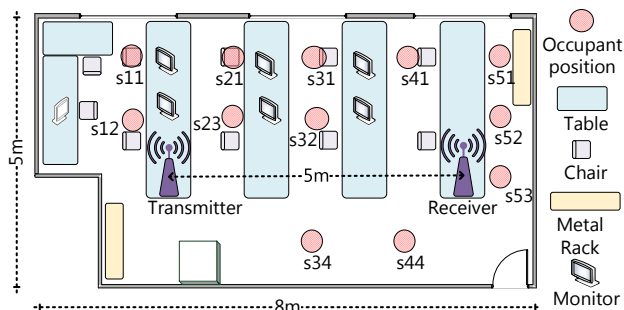


Figure 9: Floor plan of the lab. The two laptops operate as the transmitter and the receiver.

types between the transmitter and receiver, *i.e.*, A - LoS, B - NLoS. In experiment B the LoS link is blocked by multiple 15 inch computer screens. In each experiment, we collected data for three scenarios: (i) unoccupied room (serves as reference data), (ii) a stationary person, and (iii) a walking person.

For the experiments (both LoS and NLoS) involving a stationary person, 12 different positions were chosen as indicated in Figure 9. In the figure, positions are marked with  $s_{ij}$  where  $i$  is the row number and  $j$  is the column number. During this experiment, the person stays for a while in each position and is involved in subtle movements with regular pauses. In the experiments with a walking person, two scenarios are considered. In one of them, the person is not obstructing the LoS link (we name this scenario as *nld*) and in the other, the person's path crosses the link (*ldn*).

The transmitter and receiver of the experimental setup consists of two laptops, ACER 5740 and Lenovo Thinkpad L520 Both run Ubuntu version 14.04. Each of them is equipped with three external antennas. We installed a Wi-Fi card with the IEEE 802.11n IWL 5300 chipset, modified driver and firmware in the two laptops to function as the transmitter and receiver in our work. Both Wi-Fi cards in the two laptops were programmed to operate in monitor mode, which is one of the Wi-Fi modes provided by the IEEE 802.11n standard to sniff packets in a particular channel. We leveraged the CSI Tool [28] to analyse the data received from the chipset.

### 5.2 Execution

In this section we explain how we collected data from the two experiments and how we performed the dimensionality reduction and human presence detection using those data.

Altogether there were 32 measurement sets gathered for experiment A and B, each experiment consisting of 16 scenarios (12 static, 2 dynamic and 2 reference). We use the two reference data sets to calculate false positives. For each scenario, the transmitter was programmed to send packets for 60 s at 1000 pkts/s using injection scripts provided by the CSI Tool. Hence, data is collected for a total of  $16 \times 2$  scenarios amounting to a total duration of 32 minutes. To avoid interference from other devices, all measurements were collected in channel 64 which is a 20 MHz Wi-Fi channel with centre frequency 5.32 GHz. The parameters used in the experiments are provided in Table 2.

The transmission rate of 1000 pkts/s leads to a two dimensional observation CSI matrix of size  $(30 \times N_{tx} \times N_{rx}) \times (N_{obs})$  where  $N_{obs} = 60000$  for each scenario. If the observation matrix is directly transformed to the kernel matrix which is of size  $N_{obs} \times N_{obs}$ , applying PCA or kPCA requires heavy usage of system memory as  $N_{obs}$  is too large. If  $N_{obs}$  is too small, we lose the correlations in the data. Therefore, we divided each scenario of 60 s to 20 continuous subinter-

Table 2: Experiment parameters for the selected scenarios.

Parameter	Value	Parameter	Value
Environment	Cluttered	Antennas	$3 \times 3$
Exp. duration	60 s	TX power	15 dBm
# of exp.	15	Channel BW	20 MHz
Link length	5 m	Pkt TX rate	$1000 \text{ pkts}^{-1}$
Carrier freq.	5.32 GHz	$N_{obs}$	3000

vals of 3 s containing a batch of  $N_{obs} = 3000$  packets. Then we performed kPCA separately on the 20 subintervals and obtained 20 pairs of principal components and eigenvalues. There is also a practical reason for choosing  $N_{obs} = 3000$ . That is, 3000 packets correspond to 3 s which is a good response time for an occupancy detection scheme.

Thereafter, for each batch of 3000 packets, we perform kPCA with Gaussian and Polynomial kernels to determine the eigenvalues, best principal components, and calculate detection percentages. For the two environments A, B we set the parameters for the Gaussian kernel explained in Section 4.3.1 as  $Eud_{th,A} = 32$ ,  $Eud_{th,B} = 35$  respectively,  $\sigma_{unoccu} = f^{-1}(.95)$  and  $\sigma_{occu} = f^{-1}(.7)$ . A detection percentage for an experiment is  $\frac{N_{det}}{N_{int}} \times 100\%$  where  $N_{det}$  is the number of intervals that exceeds the detection threshold and  $N_{int}$  is the total number of intervals. As a comparison, we apply PCA to the same data and compare the detection percentages for the selected principal components in the following section.

### 5.3 Results Analysis

In this section, we quantify the True Positives (TP) and False Positives (FP) of our presence detection scheme. Furthermore, we assess the performance of the underlying dimension reduction techniques for static and dynamic persons. Then we evaluate the impact of the selection of principal component and observation interval ( $N_{obs}$ ) on overall detection accuracy.

#### 5.3.1 Overall detection performance

For both Gaussian kPCA and PCA in experiment A the best performing principal component in terms of detection is *PC 2*. For polynomial kPCA, *PC 3* has the best performance. However, in Experiment B, *PC 3* is consistently providing good detection percentages. It can be argued that the reason for this is the noise profile of the empty scenario in the two experiments. Since the link in experiment B is NLoS, the received signal is more noisy than in experiment A, which is a LoS link. Hence in experiment B, *PCs 1* and *2* capture this variance caused by high fluctuations in the link. Therefore, we used *PC 2* for human detection in Exp. A and *PC 3* for detection in experiment B. In Table 3, we provide the average percentages of true and false positives of all the 14 scenarios for the two experiments. On average, the Gaussian kernel has a better detection performance because of high TPs and low FPs. The reason for false positives to be zero in most cases is that we set the threshold  $\lambda_{th}$  the highest eigenvalue from the intervals of the reference

Table 3: Average detection percentages for Exp. A and B.

	PCA		G-kPCA		p-kPCA	
	TP	FP	TP	FP	TP	FP
A ( <i>PC 2</i> )	88.3%	0%	90.6%	0%	62.6%	0%
B ( <i>PC 3</i> )	83.3%	5%	88.3%	0%	62.6%	5%

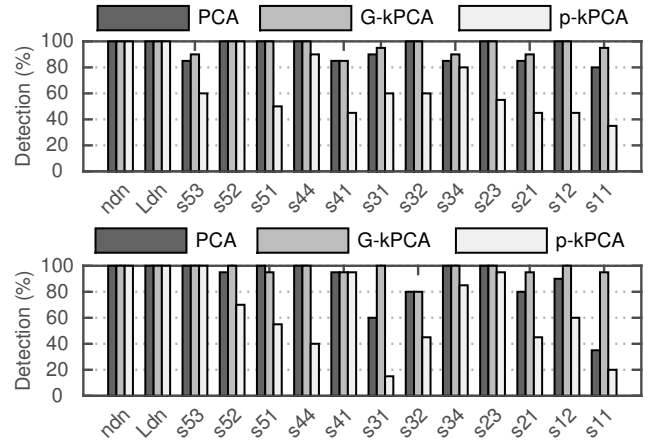


Figure 10: Scenario-wise detection percentages of experiments A (top) and B (bottom).

unoccupied room data set as explained in eq.19.

#### 5.3.2 Scenario-wise detection performance

Here we compare the performance of each technique under true detection percentages for each scenario. Figure 10 provides the detection comparison of each technique scenarios in experiments A (top) and B (bottom). We consider 14 scenarios, two dynamic (*ndn*, *ldn*) and 12 static as illustrated in Figure 9. Highest detection percentages in general are for the two dynamic scenarios and for positions near the link such as *s12*, *s23*, *s32*, *s43*, *s52* and *s53*. Lowest detections are generally for positions far away from the link such as *s11*, *s21* and *s41*.

This behaviour can be explained as follows. When a person is closer to the LoS, more paths get affected. The number of paths disturbed by the person far away from the link are less and have weak amplitudes so they do not cause large perturbations in CSI. For the two dynamic scenarios performed in the experiments, the three techniques have ideal detection rates. This highlights the fact that the selected approaches are well capable of detecting human motion.

#### 5.3.3 Performance for a static person

Here, we evaluate the detection accuracy for a static person. The two plots in Figure 10 depict that Gaussian kPCA has a consistent detection percentage in the static scenarios. Especially for the NLoS link in experiment B, the detection performance is quite above the other two. This can be attributed to the dynamic parameter adjustment for the Gaussian kPCA which was explained in detail in Section 4.3.1. This can be further verified through the analysis of *PC2* (which is  $y_i$  where  $i = 2$  as calculated in Section 4.2). As an example, the behaviour of *PC 2* for a static scenario, especially, for position *s32* is illustrated in Figure 11.

In Figure 11 *PC 2* of the Gaussian and Polynomial kPCA are compared to *PC 2* of PCA. Additionally, each figure contains *PC 2* of the unoccupied room as a reference. Since the three plots have different scales due to the use of different kernels for transformation, they are normalised by the maximum range of the occupied room's respective *PC*. The figures show that Gaussian kPCA has enhanced signal amplitude, whereas in the other two cases, the signal is immersed in noise. The reason is the suppression of noise through dynamic adjustment of  $\sigma$  in the Gaussian kPCA.

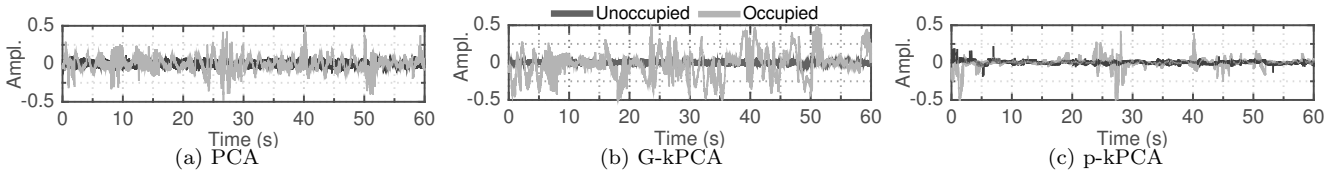


Figure 11: Comparison of temporal variation in  $PC 2$  of PCA, G-kPCA and p-kPCA for position  $s_{32}$  of experiment A.

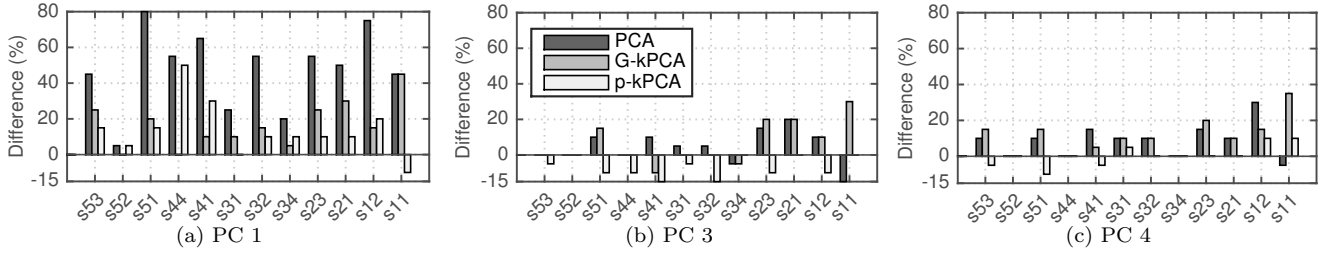


Figure 12: Detection percentage difference of  $PC 1$ ,  $PC 3$  and  $PC 4$  compared to  $PC 2$ .

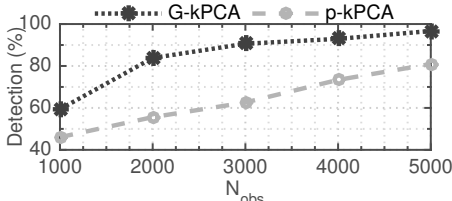


Figure 13: Impact of observation interval  $N_{obs}$  on detection.

This provides a consistently high amplitude during the presence of a person. Polynomial kPCA produces high amplitudes when there is only significant motion. For example in the 20s and 30s interval there is a sudden rise in variation. However, because we are comparing predominantly a static person in this situation, there can be only occasional movement that can cause large signal variations. Due to this reason, the Gaussian kernel performs better than the other two in mostly static situations. The Polynomial kernel has the lowest detection percentage which signifies that it requires further tweaking of its parameters.

### 5.3.4 Impact of the PC on detection

For experiment A, we selected  $PC 2$  to detect a person. Here, we show the difference in detection percentages in the other three principal components compared to that of  $PC 2$ . Figure 12 shows the detection percentage difference of the other three principal components 1, 3 and 4 compared to  $PC 2$ .  $PC 1$  has the highest difference and  $PC 3$  has the lowest for Gaussian kPCA and PCA. Although  $PC 1$  captures the highest variance fundamentally, under-performance of  $PC 1$  in terms of detection is due to the capture of noise in the unoccupied environment as explained in Section 4.4.

### 5.3.5 Impact of the observation interval on detection

In our detection scheme, we selected  $N_{obs} = 3000$  which consists of 3s intervals as the number of observations to perform dimensionality reduction and human detection. Here we evaluate the impact of  $N_{obs}$  on presence detection for our schemes Gaussian kPCA and Polynomial kPCA. Figure 13 illustrates the detection percentage variation with increase of  $N_{obs}$  for a single scenario in experiment A.

Summarising the results, we can state that human detection based on Gaussian kPCA is quite efficient in adverse conditions such as stationary users and NLoS links. Although the Polynomial kPCA based approach detects human motion, it requires further tweaking of parameters.

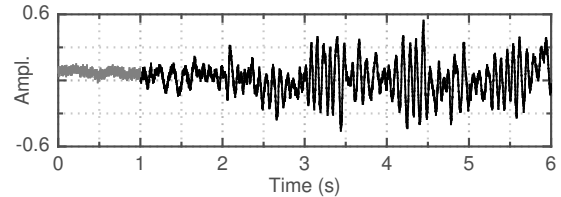


Figure 14: Temporal variation of  $PC 2$  of a walking person in Section 3.3 after applying G-kPCA to reduce dimensions.

## 6. DISCUSSION

This section discusses limitations and possible augmentations to our dimensionality reduction techniques and the human presence detection scheme. Our work explored only the efficient usage of CSI amplitude on human presence detection through non-linear techniques. However, the phase response can also be incorporated in the detection, especially given that the correlation between amplitude and phase are non-linear. Our detection approach requires prior knowledge of the environment to determine principal components, thresholds and to adjust parameters. Since we are using non-linear dimensionality reduction techniques, the computational complexity increases with the observation interval,  $N_{obs}$ . However, the advantage of these techniques is that the complexity is not dependant on the number of dimensions. Here we did not analyse the detection performance of our scheme in the presence of multiple occupants. However, in such a situation we expect high detection performance from this system compared to a single person because multiple persons create more movements and disrupts more paths than a single person.

With enhanced detection accuracy provided especially by the Gaussian kernel, this non-linear technique can be extended to multiple occupant detection and activity recognition. As an example for an activity recognition scenario, in Figure 14 we plot the second PC of the experiment performed to validate the human presence detection model in Section 3. During this experiment, the person's trajectory lies perpendicular to the link. We plot the person's movement during the interval 1s–6s, as a reference, occupied room noise is plotted during the interval 0s–1s.

## 7. CONCLUSIONS

In this work, we provided a model-based approach to detect human presence using CSI provided by off-the-shelf

Wi-Fi chipsets. First we modelled the effect of humans on CSI amplitude and using this model, we analysed the non-linearities among CSI sub-carrier amplitudes. We then exploited those non-linearities efficiently by introducing non-linear techniques to reduce CSI dimensions and then detected human presence with just two Wi-Fi transceivers. We explored the overall detection performance of our system through true and false positives and evaluated the detection scheme's potential especially for detecting a static person. We showed that especially the Gaussian kernel can achieve a higher detection performance than the linear approach. Finally, we demonstrated that this technique can be extended to activity recognition as well.

## 8. ACKNOWLEDGMENTS

This work has been funded by the Irish Research Council and United Technologies Research Centre, Cork, Ireland. We thank Ramona Marfievici and Pablo Corbalán for providing insightful comments.

## 9. REFERENCES

- [1] Tero Kivimaki et al. A Review on Device-Free Passive Indoor Positioning Methods. *International J. of Smart Home*, 08(1):71–94, 2014.
- [2] Thiago Teixeira et al. A survey of human-sensing: Methods for detecting presence, count, location, track, and identity. *ACM Comput. Surv.*, 5:1–77, 2010.
- [3] Kelly Caine et al. The effect of monitoring by cameras and robots on the privacy enhancing behaviors of older adults. In *Proc. of HRI*, 2012.
- [4] O. Kaltiokallio et al. Follow @grandma: Long-term device-free localization for residential monitoring. In *Proc. of LCN Workshops*, 2012.
- [5] Zheng Yang et al. From rssi to csi: Indoor localization via channel response. *ACM Comput. Surv.*, 46(2):25:1–25:32, December 2013.
- [6] Z. Zhou et al. Towards omnidirectional passive human detection. In *Proc. of INFOCOM*, 2013.
- [7] Jiang Xiao et al. Fimd: Fine-grained device-free motion detection. In *Proc. of ICPADS*, 2012.
- [8] N. Patwari and J. Wilson. RF Sensor Networks for Device-Free Localization: Measurements, Models, and Algorithms. *Proc. of the IEEE*, 98(11):1961–1973, 2010.
- [9] Neal Patwari and Joey Wilson. People-Sensing Spatial Characteristics of RF Sensor Networks. *CoRR*, abs/0911.1972, 2009.
- [10] Wei Wang et al. Understanding and Modeling of WiFi Signal Based Human Activity Recognition. In *Proc. of MobiCom*, 2015.
- [11] Jiang Xiao et al. Pilot: Passive device-free indoor localization using channel state information. In *Proc. of ICDCS*, 2013.
- [12] Liangyi Gong et al. An adaptive wireless passive human detection via fine-grained physical layer information. *Ad Hoc Networks*, 2015.
- [13] Fu Xiao et al. Invisible Cloak Fails: CSI-based Passive Human Detection. In *Proc. CSAR*, 2015.
- [14] Z. Zhou et al. Omnidirectional Coverage for Device-Free Passive Human Detection. *IEEE Trans. on Parallel and Distributed Systems*, 25(7):1819–1829, July 2014.
- [15] Yossi Rubner and Carlo Tomasi. *Perceptual metrics for image database navigation*, volume 594. Springer Science & Business Media, 2013.
- [16] Kun Qian et al. Pads: passive detection of moving targets with dynamic speed using phy layer information. In *Proc. of ICPADS*, 2014.
- [17] Chenshu Wu et al. Non-Invasive Detection of Moving and Stationary Human With WiFi. *IEEE J. on Selected Areas in Communications*, 33(11):2329–2342, 2015.
- [18] H. Hashemi. The indoor radio propagation channel. *Proc. of the IEEE*, 81(7):943–968, July 1993.
- [19] Kaishun Wu et al. Fila: Fine-grained indoor localization. In *Proc. of INFOCOM*, 2012.
- [20] David Tse and Pramod Viswanath. *Fundamentals of wireless communication*. Cambridge University Press, 2005.
- [21] Daniel Halperin et al. Predictable 802.11 packet delivery from wireless channel measurements. *ACM SIGCOMM Comput. Commun. Rev.*, 41(4), August 2010.
- [22] Deepak Vasisht et al. Decimeter-level localization with a single wifi access point. In *Proc. of the NSDI*, 2016.
- [23] Souvik Sen et al. Precise indoor localization using phy layer information. In *Proc. of Hot Topics in Networks*, 2011.
- [24] Bernhard Schölkopf et al. Advances in kernel methods. chapter Kernel Principal Component Analysis, pages 327–352. 1999.
- [25] Sebastian Mika et al. Kernel PCA and De-noising in Feature Spaces. In *Proc. of Advances in Neural Information Processing Systems II*, 1999.
- [26] Quan Wang. Kernel Principal Component Analysis and its Applications in Face Recognition and Active Shape Models. *CoRR*, abs/1207.3538, 2012.
- [27] Alex J Smola et al. The connection between regularization operators and support vector kernels. *Neural networks*, 11(4):637–649, 1998.
- [28] Daniel Halperin et al. Tool release: gathering 802.11n traces with channel state information. *ACM SIGCOMM Comput. Commun. Rev.*, 41(1):53–53, 2011.